Modeling of fault gouges with Cosserat Continuum Mechanics: Influence of thermal pressurization and chemical decomposition as coseismic weakening mechanisms

Emmanuil Veveakis, Jean Sulem, Ioannis Stefanou

Modeling of fault gouges with Cosserat Continuum Mechanics: Influence of thermal pressurization and chemical decomposition as coseismic weakening mechanisms

Emmanuil Veveakis*

National Technical University of Athens, School of Applied Mathematics and Physics, Theocharis Bld, Iroon Politechniou 5, Zografou, Athens, 15773, Greece

Jean Sulem

UR Navier-CERMES, Ecole des Ponts ParisTech, Université Paris-Est, 6,8 Avenue Blaise Pascal, Champs-sur-Marne, 77455, Marne-la-Vallée Cedex 2, France

Ioannis Stefanou

National Technical University of Athens, School of Applied Mathematics and Physics, Theocharis Bld, Iroon Politechniou 5, Zografou, Athens, 15773, Greece

Abstract

In this paper we study the impact of thermal pressurization and mineral decomposition reactions under seismic deformation conditions (e.g., slip rates of about 1 m/s) triggered by shear heating, to the stability of a saturated fault material. By using higher order continuum considerations, allowing for rotational degrees of freedom to the gouge material, we verify that the micro-inertia of the Cosserat continuum may regularize the ill-posed problem of simple shear of a fault and that the thermal effects promote localization of deformation into ultra-thin shear bands. It is shown that the width of these

*Corresponding Author. Email: manolis@mechan.ntua.gr, Tel:+30 210 772 1373

structures depends on the parameters of the decomposition reaction considered, obtaining values as low as 100 μm, in agreement with microstructural evidence from natural and artificial faults. .
Key words: *Shear Heating*, *Cosserat Continuum*, *Reaction kinetics*, *Undrained adiabatic shearing*, *Micro-Inertia*

1. Introduction

Geomaterials exhibit failure in various patterns, like the propagation of single fractures in otherwise intact rock, crack growth in presence of multiple interacting fractures, initiation and percolation of damage zones under quasi-static and dynamic loading, strain localization into shear- or compaction bands.

The theory describing localized failure has been a direct extension of the classic Mohr's strength of materials theory, and is applied for geomaterials using the so-called Thomas - Hill - Mandel shear-band model (Hill (1962); Mandel (1966)), which was introduced in the early 60s and it was widely publicized by the paper of Rudnicki and Rice (1975). More recently, the mathematical formulation of bifurcation and post-bifurcation phenomena and related instabilities was summarized by Vardoulakis and Sulem (1995) to form the basis of a contemporary continuum theory of failure of geomaterials.

Apart from the theoretical point of view of failure, shear banding has been claimed as the primary failure pattern for faults (Rice (2006)) and landslides (Vardoulakis (2002a)). However, field evidence from exhumed faults reveals that seismic events take place in even narrower zones within shear-bands, formed from post-failure evolution (Chester and Chester (1998)), dominated

by weakening mechanisms that are considered to be mainly thermal of origin (Rice (2006)). Indeed, field observations suggest that slip in individual events may then be extremely localized, and may occur primarily within a thin shear zone, $< 1 - 5\ mm$ thick, called the principal slipping zone (PSZ) (Sibson (2003)). This localized shear zone lies within a finely granulated fault core of typically tens to hundreds millimeter thickness, as shown schematically in the idealized description of Fig. 1.

Evidence for that morphology can be found in the North Branch San Gabriel fault (Chester et al. (1993)) and Punchbowl (Chester and Chester (1998)) fault of the San Andreas system in southern California, the Median Tectonic Line fault in Japan (Wibberley and Shimamoto (2003)), and in the Hanaore fault in southwest Japan (Noda and Shimamoto (2005)). Note also that from drilling cores in the Aigion system, central Greece, the fault core of clay size particles consisting of finely crushed radiolarites, extended to about $1\ m$, was found to be intercepted by a "fresh"distinct slip surface of sub-millimiter size (Sulem (2007); Cornet et al. (2004)).

As perhaps the best characterized case, a thin principal slipping zone was identified along an exposure of the Punchbowl fault at 2 to 4 km depth, which has accommodated 44 km of slip (Chester and Chester (1998)). Also, a thin central slip zone was identified by Wibberley and Shimamoto (2003) along the Median Tectonic Line fault. The nominal thickness of such a shear zone is usually of the order of sub-millimeter and, as described by Smith et al (2011), it could be met in calcite-bearing fault rocks even in the absence of pressure-solution and precipitation, providing thus field evidence of extreme localization during coseismic slip in natural faults. On the other hand the

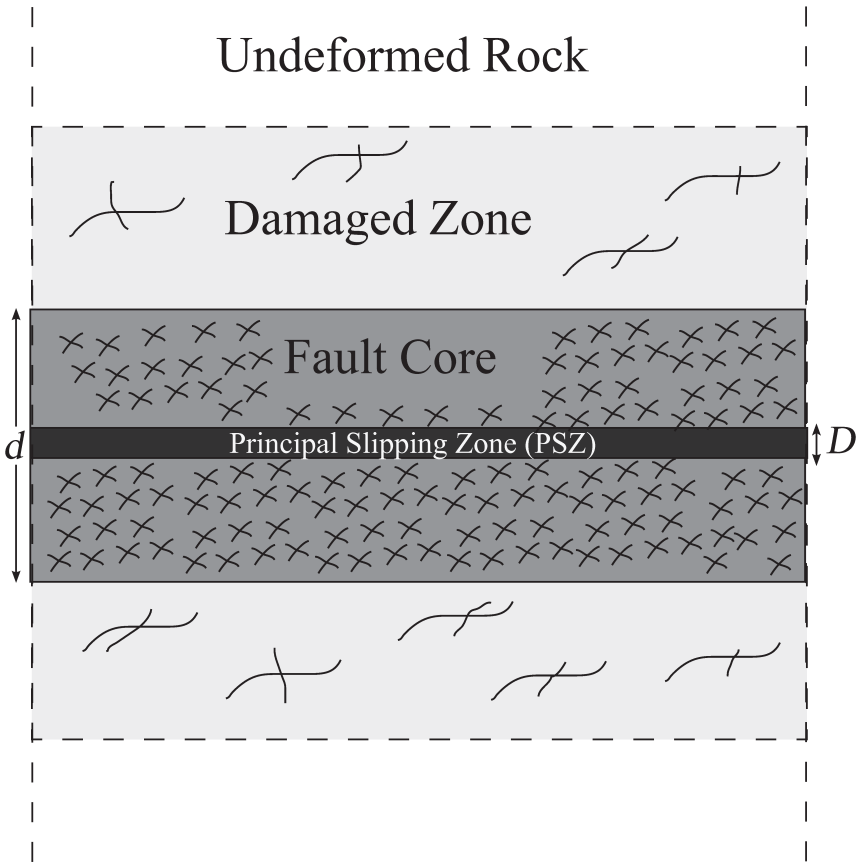

Figure 1: Idealized description of a natural fault zone, as presented by Chester et al. (1993) and Wibberley et al. (2008). The fault core, d, is of the order of centimeters, whereas the Principal Slipping Zone (PSZ) D is of the order of millimeter or less.

thickness of the cataclastic core may vary up to a few centimeters.

In geomechanics there are several studies focusing on the thickness of shear bands in soils. Morgenstern and Tschalenko (1967) calculated that shear bands for a clay, kaolin may have thicknesses of order $10 - 100$ times a clay platelet size ($\sim 0.5\,\mu m$). For granular materials on the other hand usually use the mean particle diameter, d_{50}, is used as a scaling measure, defined for nonuniform size distributions such that 50 % by weight of the particles have larger size.

Under purely mechanical effects, Muhlhaus and Vardoulakis (1987) calculated for sands the thickness of the initial shear band (with thickness d in Figure 1) to be around $d \sim 16 d_{50}$. In any case, this zone seems to be rather wide to be considered as the primary slip surface (Rice (2006)). Indeed, Chester and Goldsby (2003) showed that the nominal thickness of the Punchbowl's cataclastic core varies from 0.6 to 1.1 mm. However, as Rice (2006) mentions: "*within this* ~ 1 *mm thick nominal shear zone, most of the shearing seems to have been accommodated within a zone of extreme shear localization having an apparent thickness of* $100 - 300\,\mu m$ ". Rice (2006) showed that d_{50} is not always a characteristic length scale for cataclastic and ultracataclastic formations, since apparently $d_{20} - d_{30}$ seems to be more appropriate for modeling the PSZ. Thus, in principle the PSZ represents a very fine shear localization, consisting of ultrafine particles that have usually undergone mechano-chemical degradation (gelification, decarbonation and dehydration reactions, melting, as thoroughly discussed by Di Toro et al. (2011)). Therefore, other mechanisms that are responsible for the formation of these structures and the dynamic weakening of faults should be looked

after.

Since fault zones usually exhibit the presence of fluid interacting with the rock, hence inducing coupled effects including shear heating and pore fluid pressurization, such mechanisms are expected to act as weakening mechanisms during fault slip (Sibson (1973); Lachenbruch (1980); Wibberley and Shimamoto (2005)). These mechanisms have also been suggested for weakening in catastrophic landslides (Vardoulakis (2002a); Veveakis et al. (2007); Goren and Aharonov (2007); Pinyol and Alonso (2010); Goren et al. (2010)). Thermo-poro-mechanical couplings due to shear heating (Sulem et al. (2005); Rice (2006)) can be also associated to chemical effects such as dehydration of minerals or decomposition of carbonates, theoretically studied recently by Brantut et al. (2010, 2011); Sulem and Famin (2009); Veveakis et al. (2010) and reported to take place in real faults (Hirono et al. (2007)) and experiments at laboratory conditions (Han et al. (2007); Ferri et al. (2010); Brantut et al. (2011a); De Paola et al. (2011)).

In a recent paper, Sulem et al. (2011) have shown that by resorting to a Cosserat continuum (Vardoulakis and Sulem (1995)) for describing the kinetics of a granular material, a preferred wave length for the instability mode of a layer under shear can be selected. They showed that instability can occur even in the hardening regime of the stress-strain curve, due to thermal pressurization, confirming the claim that thermal in origin mechanisms play a major role in the formation and evolution of the PSZ. The localizing structures obtained were comparable in thickness with the ones observed in nature, rationalizing thus the viscous and second gradient regularization initially proposed by Vardoulakis (1985, 1986, 1996) for regularizing these type

of problems. In this work we extend this analysis by including chemical reactions that may take place inside a rapidly deformed shear-band and study the impact of certain decomposition reactions to the dynamic weakening and localization of deformation in granular media.

2. Problem Formulation

In classical Continuum mechanics, where the continuum is allowed only for translational degrees of freedom (displacements), one may be able to predict the onset of a shear band (Rudnicki and Rice (1975)). However it can be shown that the instability tends to localize in a strip of zero thickness. Classical theories are thus unable to simulate the localization of the deformation in a shear band of finite thickness. This drawback can be traced back to the fact that conventional constitutive models do not contain material parameters with dimension of length which can scale the shear band thickness (internal length).

Thus, a fault is usually modelled as a discontinuity surface for the velocity fields. Such an oversimplifying assumption however would overestimate significantly the heat produced in a fault, and thus the temperature (as shown by Rice (2006)), imposing difficulties in our effort to determine the processes taking place during dynamic weakening of faults. To raise this discrepancy, the introduction of a thin but finite-in-width slipping zone of intense shear is requested. Vardoulakis (1985, 1986, 1996) showed that introducing viscous (rate-dependent) considerations, combined with second gradient plasticity models, may alleviate the ill-posedness of the problem. Later, Veveakis et al. (2010) showed that indeed non-linear viscous responses provide the necessary

counterbalancing effect to stabilize the problem of simple shear.

Early approaches by Hill (1962) and Mandel (1966) envisioned such a structure with width d, which however could only be artificially imposed, since -as said before- in classical continua d is undetermined. It seemed as if the solutions obtained from classical continua correspond to the limit $d \to 0$ of a corresponding higher grade extension of it (see Vardoulakis and Sulem (1995), p. 268 for a comprehensive discussion). Following this conclusion, as well as experimental observation of the influence of the effect of particle irregularities and rotations inside the shear bands, Muhlhaus and Vardoulakis (1987) resorted to concepts from Cosserat Continuum mechanics to naturally determine d. Thus, by allowing both particle displacements and particle rotations, they accounted for the angularities of the grains, and enriched the classical continuum with additional kinematic and static fields, and calculated for sands that $d \sim 16 d_{50}$. Other mechanisms leading to localization, and initially neglected by Muhlhaus and Vardoulakis (1987), are reported to be flash heating and powder lubrication (Di Toro et al. (2011); De Paola et al. (2011); Han et al. (2010, 2011); Tisato et al. (2011)) or grain breakage (Nguyen and Einav (2010)).

In this study we follow Muhlhaus and Vardoulakis (1987) and consider a layer of saturated granular material of thickness D that is sheared in plane strain (Fig. 2) in such a way that there is no extensional strain in the x_1 -direction and displacements u_1 and u_2 of material points vary only with x_2 (and time t). The additional rotational degree of freedom of the considered 2D Cosserat continuum is ω_c. The grains themselves are not allowed for breakage or wear, excluding thus breakage and flash heating, since the scope

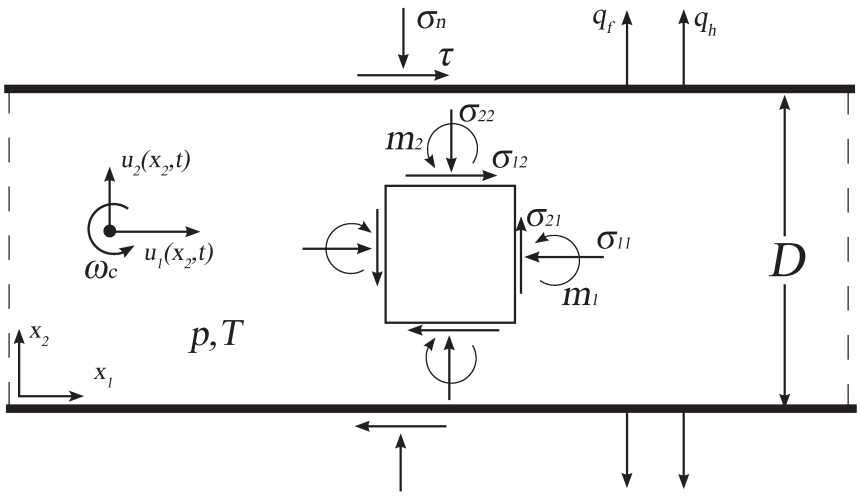

Figure 2: Problem formulation. Cosserat stresses, couple stresses and degrees of freedom.

of this study is to provide insights on the thickness of the PSZ at different temperature regimes.

2.1. Constitutive equations of elasto-plasticity

The incremental constitutive equations for the considered 2D Cosserat continuum are derived from the Muhlhaus - Vardoulakis plasticity model (Muhlhaus and Vardoulakis (1987)). The main feature of the model is that a 2D flow theory of plasticity for granular media with Cosserat microstructure can be derived by keeping the same definitions for the yield surface and the plastic potential as in the classical theory and by generalizing appropriately

the stress and strain invariants involved in these definitions. The details of the model for isothermal deformation are given in Vardoulakis and Sulem (1995) and in Sulem et al. (2011). They are briefly recalled in the following.

In a two-dimensional Cosserat Continuum each material point has two translational degree of freedom (v_1, v_2) and one rotational degree of freedom $\dot{\omega}_c$. The four components of the rate of the non-symmetric deformation tensor are given as

$$\dot{\epsilon}_{11} = \frac{\partial v_1}{\partial x_1} \; ; \; \dot{\epsilon}_{12} = \frac{\partial v_1}{\partial x_2} + \dot{\omega}_c \qquad (1)$$
$$\dot{\epsilon}_{21} = \frac{\partial v_2}{\partial x_1} - \dot{\omega}_c \; ; \; \dot{\epsilon}_{22} = \frac{\partial v_2}{\partial x_2},$$

and the two components of the curvature of the deformation rate (gradient of the Cosserat rotation rate)

$$\dot{\kappa}_1 = \frac{\partial \dot{\omega}_c}{\partial x_1} \; ; \; \dot{\kappa}_2 = \frac{\partial \dot{\omega}_c}{\partial x_2}. \qquad (2)$$

Moreover we decompose the stresses and strain rates into spherical and deviatoric parts, $\sigma_{ij} = s_{ij} + \sigma_{kk}\delta ij/2$ and $\dot{\epsilon}_{ij} = \dot{e}_{ij} + \dot{\epsilon}_{kk}\delta_{ij}/2$, where δ_{ij} is the Kronecker's delta. The following generalized stress and strain invariants are used:

$$\sigma = \frac{\sigma_{ii}}{2} \; ; \; \tau = \sqrt{h_1 s_{ij} s_{ij} + h_2 s_{ij} s_{ji} + h_3 m_k m_k / R} \qquad (3)$$
$$\dot{\epsilon}^p = \dot{\epsilon}^p_{kk} \; ; \; \dot{\gamma}^p = \sqrt{g_1 \dot{e}^p_{ij} \dot{e}^p_{ij} + g_2 \dot{e}^p_{ij} \dot{e}^p_{ji} + R^2 g_3 \dot{\kappa}_k \dot{\kappa}_k},$$

where $h_i = [3/4, -1/4, 1]$, $g_i = [3/2, 1/2, 1]$ for the so-called static Cosserat model, and R is the internal length (Vardoulakis and Sulem (1995)).

Besides the four components of the non-symmetric stress-tensor σ_{ij}, there are two couple stresses m_k $(k = 1, 2)$. As in classical small-strain plasticity theory, the deformation is decomposed into elastic and plastic parts

$$\dot{\epsilon}_{ij} = \dot{\epsilon}^e_{ij} + \dot{\epsilon}^p_{ij} \ ; \ \dot{\kappa}_k = \dot{\kappa}^e_k + \dot{\kappa}^p_k. \tag{4}$$

Following Sulem et al. (2011) we assume a Terzaghi decomposition of the stress tensor in effective stress and pore pressure ($\sigma_{ij} = \sigma'_{ij} - p\delta_{ij}$) and assume a Coulomb yield stress and plastic potential for the effective stresses:

$$\begin{aligned} F &= \tau + \mu(\sigma + p), \\ Q &= \tau + \beta(\sigma + p), \end{aligned} \tag{5}$$

where the mobilized friction coefficient μ and the dilatancy coefficient β are functions only of the accumulated plastic strain γ^p. Under these considerations, the rate thermo-poro-elasto-plastic relationships are expressed as follows

$$\begin{aligned} \dot{\gamma} &= \frac{\dot{\tau}}{G} + \dot{\gamma}^p \\ \dot{\epsilon} &= \frac{1}{K}(\dot{\sigma} + \dot{p}) + \alpha_s \dot{T} + \dot{\epsilon}^p, \end{aligned} \tag{6}$$

where G and K are the elastic shear and bulk modulus respectively, α_s the thermal dilation coefficient of the solid skeleton and T the temperature. The

rate of plastic deformation is written as

$$\dot{\gamma}^p = \frac{1}{H}\left[\dot{\tau} + \mu(\dot{\sigma} + \dot{p})\right] \; ; \; \dot{\epsilon}^p = \beta\dot{\gamma}^p, \tag{7}$$

where $H = H(\gamma^p) = h(\sigma + p)$ (with $h = d\mu/d\gamma^p$) is the plastic hardening modulus, which is related to the tangent modulus H_{tan} of the τ versus γ curve through the relationship $H_{tan} = \frac{H}{1+H/G}$ and is either positive or negative according to whether the $\tau - \gamma$ curve is increasing (hardening) or decreasing (softening). Notice that, in principle H_{tan} is varying with strain, as thoroughly presented by Rudnicki and Rice (1975). When H_{tan} is non positive then the material is enterring an unstable regime, where softening induces localization of deformation in a shear band (Holcomb and Rudnicki (2001)). However, when the material is fluid saturated (Sulem et al. (2011)), thermal pressurization may cause localization of deformation even at hardening regimes, before reaching $H_{tan} = 0$, where the material is supposed to be stable. In this work we study the effect of a chemical reaction at high temperatures, near the activation temperature of the reaction, to assess whether the reaction itself may induce softening and localization at even higher values of the hardening modulus.

2.2. Stress Equilibrium

For the considered 2D Cosserat continuum and the configuration of Fig. 2, the local equilibrium equations are

$$\begin{aligned} \frac{\partial \sigma_{12}}{\partial x_2} &= 0, \\ \frac{\partial \sigma_{22}}{\partial x_2} &= 0, \\ \frac{\partial m}{\partial x_2} + \sigma_{21} - \sigma_{12} &= 0, \end{aligned} \tag{8}$$

where $m = m_2$ and $m_1 = 0$. The stresses applied at the boundary are a shear stress τ and a normal stress σ_n in the x_2 direction. It is assumed that no couple stress is imposed at the boundary. Prior to localization, the state of stress and strain is uniform and considering the couple free boundary condition, the couple stress is identically zero in the sheared layer. Therefore the rock behaves as a classical continuum before localization.

2.3. Reaction kinetics

We assume the presence of a decomposition reaction that decomposes the solid skeleton and produces excess pore fluid. In particular, as an example we consider the reaction of calcite decomposition ($CaCO_3 \rightarrow CaO + CO_2$), producing CO_2 which at high pressures and temperatures (conditions similar to the ones met in faults at depth) is at supercritical, liquid state (Sulem and Famin (2009)). Evidence of the presence of this reaction in faults is found in many active crustal faults (Famin et al. (2008)), and experimentally reproduced for example by Han et al. (2007) from experiments on simulated

faults in Carrara marble. Other types of chemical reactions such as mineral dehydration (Brantut et al. (2011)) could be studied following the same methodology.

Following Sulem and Famin (2009) and Veveakis et al. (2010), we assume that the reaction is taking place with a rate r, which on its turn can be expressed from first order reaction kinetics as (Law (2006))

$$r \approx \frac{\rho_s}{M_{\mathrm{CaCO_3}}} A_0 e^{-T_c/T}, \tag{9}$$

where $T_c = E/R_a$ the activation temperature of the reaction, E the activation energy and R_a the universal gas constant. In this expression A_0 is the pre-exponential factor, a parameter that may vary significantly, obtaining for calcite decomposition values between $10^2 s^{-1}$ and $10^{20} s^{-1}$ (Lvov et al. (2002)).

The Arrhenius model assumed in Eq. (9), is the simplest one, but has received much criticism for its validity, mainly due to the strongly varying magnitudes of both A_0 and T_c for a given reaction (Lvov et al. (2002)). In the pertinent literature there are numerous models suggested to replace it (Law (2006), pp. 67-72) for evaluating the reaction rate of a decomposition reaction. Lvov et al. (2002) provide a comprehensive literature guide through the models used, along with experimental data for calcite decomposition. Even for this well reported reaction, the production rates are measured through experiments at zero or very low pressures, of the order of $mbar$. Nonetheless it is known that pressure reduces significantly the rate of a reaction (Lvov (2007), pp. 79), hence when applying to geomechanical problems, one would need experimental data of calcite decomposition at pressures of the order of several tens of MPa. To our knowledge, such information is not available in the literature.

Apart from the pressure dependency of the production rates, we need to emphasize that the activation energy of a reaction also varies with grain size and the deformation history of a material. In the case of calcite, when the grain size decreases from $2-5$ micron to 40 nm (a grain size typically found in high speed experiments performed on limestones (Tisato et al. (2011); Han et al. (2007, 2011); De Paola et al. (2011)), the activation energy for the reaction decreases from $200\,kJ/mol$ to $130\,kJ/mol$ (see Table 1 in Yue et al (1999)), even without plastic deformation of the particles. Thus, T_c could be temperature dependent on itself, correlating the nanoparticles produced with the chemical reaction (due to chemical precipitation, Yue et al (1999)), unlike the plastically deformed nanoparticles produced in high speed experiments. The internal plastic deformation induced by milling during frictional sliding might further reduce the activation energy of the reaction (Fisher. (1988)). Hence, emphasis should be given on thorough experimental detemination of the reaction parameters at various temperature and pressure regimes.

2.4. Fluid-mass Conservation

Following the decomposition of the plastic strain rates into elastic and plastic parts (Eq. 4), we consider the volumetric plastic strain rate to consist of a mechanical part $\dot{\epsilon}^p_m$ subject to the constitutive behavior of Eq. 7 and a chemical part $\dot{\epsilon}^p_c$, influenced by the reaction rate r

$$\dot{\epsilon}^p = \dot{\epsilon}^p_m + \dot{\epsilon}^p_c. \tag{10}$$

Under the above considerations and by assuming that the solid matrix is plastically incompressible, the diffusion-reaction equation for the pore pressure

is obtained from the fluid mass equation as (Sulem and Famin (2009))

$$\frac{\partial p}{\partial t} = c_{hy}\frac{\partial^2 p}{\partial x_2^2} + \Lambda\frac{\partial T}{\partial t} - \frac{\beta}{\beta^\star}\frac{\partial \dot{\gamma}^p}{\partial t} + \frac{\rho_s - \rho_f\zeta}{\rho_f\beta^\star}\frac{A_0}{M_{\mathrm{CaCO_3}}}e^{-T_c/T}, \tag{11}$$

where $\zeta = \frac{M_{\mathrm{CaCO_3}}}{M_{\mathrm{CO_2}}} - \frac{\rho_{\mathrm{CaCO_3}}}{\rho_{\mathrm{CaO}}}\frac{M_{\mathrm{CaO}}}{M_{\mathrm{CO_2}}}$, ρ_i the density of the $i-$th constituent and ρ_s the density of the solid skeleton, c_{hy} the hydraulic diffusivity, $\beta^\star$ the storage capacity and $\Lambda = (\lambda_f - \lambda_n)/\beta^\star$ the pressurization coefficient, expressed as the difference of the thermal expansion coefficimobilizedents of the fluid (λ_f) and the pore volume (λ_n).

2.5. Heat Equation

By assuming that all the mechanical work input is converted into heat (Chester et al. (2005); Pittarello et al. (2008)), and that the heat is expressed through Fourier's law, we may obtain the diffusion-reaction temperature equation (Sulem and Famin (2009); Veveakis et al. (2010))

$$\frac{\partial T}{\partial t} = c_{th}\frac{\partial^2 T}{\partial x_2^2} + \frac{1}{\rho C}\tau\dot{\gamma}^p - \frac{|\Delta H|}{\rho C}\frac{\rho_s}{M_{\mathrm{CaCO_3}}}A_0 e^{-T_c/T}, \tag{12}$$

where c_{th} is the thermal diffusivity, ρC the specific heat capacity of the mixture and $|\Delta H| \approx E$ the specific enthalpy of the reaction, expressing the energy consumed during an endothermic reaction.

3. Undrained-adiabatic limit

The first approximation in our effort to assess the influence of these weakening mechanisms during earthquake slip is to prohibit drainage and heat flux at the boundaries of the layer ($q_f = q_h = 0$). This case corresponds to the well known undrained-adiabatic limit, acknowledged to be established at or

near seismic rates, i.e. when the heat production rate and pore pressure increase in the slipping zone is significantly larger than the heat and pore pressure diffusion times towards the fault core and in the damage zone (Garagash and Rudnicki. (2003a,b)). It provides a first insight on the impact of each mechanism on the dynamic weakening of faults. The actual value of heating rate required for the onset of the weakening mechanisms varies with the material of the fault gouge (Di Toro et al. (2011)).

In addition to the above, we assume that the normal stress σ_n acting on the sheared layer is constant. From Eqs. (7),(11),(12) we may obtain the following relationship between the shear stress rate, the strain rate and the temperature rate:

$$\dot{\tau} = \frac{\bar{H}}{1+\bar{H}/G}\dot{\gamma} + \frac{\bar{B}}{1+\bar{H}/G}\dot{T}, \tag{13}$$

where

$$\bar{H} = H + \mu\frac{\beta}{\beta^\star} - \mu\tau\left(\frac{1}{\beta^\star|\Delta H|}\frac{\rho_s - \zeta\rho_f}{\rho_f}\right), \tag{14}$$
$$\bar{B} = \mu\left(\frac{\rho C}{\beta^\star|\Delta H|}\frac{\rho_s - \zeta\rho_f}{\rho_f} - \Lambda\right).$$

Obviously, when the thermal effects are neglected (i.e. in the absence of thermal pressurization and chemical reaction) and incompressible solid and fluid are assumed (so that $\beta^\star = 1/K$) the classical expression for dilatant hardening effect, as proposed by Rice (1975) is retrieved

$$\dot{\tau} = \frac{H + \mu\beta K}{1 + (H + \mu\beta K)/G}\dot{\gamma}. \tag{15}$$

For dilatant material ($\beta > 0$) we may recognize in (13) a hardening effect due to dilatancy with the term $\mu\beta/\beta^\star$ and a strong softening effect from the

reaction due to the term $\frac{\mu\tau}{\beta^\star}\left(\frac{\rho_s-\zeta\rho_f}{\rho_f|\Delta H|}\right)$ (positive for calcite decomposition, as shown by Sulem and Famin (2009)).

As shown by Sulem et al. (2011), in the absence of a chemical reaction instability may occur even in the hardening regime of the $\tau-\gamma$ curve ($H>0$) if the dilatancy effect is very weak (as it is the case at great depth) and if the thermal pressurization effect is significant. Here we verify this claim and indicate that the presence of a chemical reaction may lead to instability at even higher hardening regimes.

4. Linear Stability Analysis of undrained adiabatic shearing of a Cosserat layer

At any given state, the evolution time of the kinematic quantities, the pore fluid pressure and the temperature determine the stability of the shearing of the Cosserat layer. The small perturbations considered herein are defined as follows:

$$\begin{aligned} u_1(x_2,t) &= u_1^0(x_2,t)+\tilde{u}_1(x_2,t), \\ u_2(x_2,t) &= u_2^0(x_2,t)+\tilde{u}_2(x_2,t), \\ \omega_c(x_2,t) &= \omega_c^0(x_2,t)+\tilde{\omega}_c(x_2,t), \\ p(x_2,t) &= p^0(x_2,t)+\tilde{p}(x_2,t), \\ T(x_2,t) &= T^0(x_2,t)+\tilde{T}(x_2,t). \end{aligned} \tag{16}$$

The governing equations for the perturbed fields ($\tilde{u}_1$, $\tilde{u}_2$, $\tilde{\omega}_c$, $\tilde{p}$, $\tilde{T}$) are of the same form as the ones derived in the previous section. Similarly, the fluid

and heat fluxes are prevented at the boundaries of the layer. However, the internal fluid and heat flows are permitted inside the layer.

4.1. Normalized equations

The system of equations can be brought in a dimensionless form by introducing the dimensionless quantities:

$$x = \frac{x_1}{R}\ ,\ z = \frac{x_2}{R}\ ,\ \bar{u}_i = \frac{u_i}{R}\ , \tag{17}$$
$$\bar{p} = \frac{p}{\sigma_n}\ ,\ \bar{\sigma}_{ij} = \frac{\sigma_{ij}}{\sigma_n}\ ,\ \bar{t} = \frac{c_{th}}{R^2}t\ ,\ \bar{T} = \frac{\Lambda}{\sigma_n}T,$$

where R is the internal length of the Cosserat model, which can be related to the mean grain size $R = d_{50}/2$. The linearized forms of the pore pressure and heat equation (linearized around $T^0 = T_c$, i.e. at higher temperature regimes, near the activation temperature of the reaction) may be reduced in their dimensionless forms as (the superimposed bars are omitted for convenience):

$$\frac{\partial p}{\partial t} = \eta\frac{\partial^2 p}{\partial z^2} + \frac{\partial T}{\partial t} + \delta\frac{\partial \dot{\gamma}^p}{\partial t} + \chi\frac{T - T_c}{T_c}, \tag{18}$$
$$\frac{\partial T}{\partial t} = \frac{\partial^2 T}{\partial z^2} + \alpha\frac{\partial \dot{\gamma}^p}{\partial t} - \psi\frac{T - T_c}{T_c},$$

where

$$\eta = \frac{c_{hy}}{c_{th}}\ ,\ \delta = \frac{\beta}{\beta^\star\sigma_n}\ ,\ \alpha = \frac{\Lambda\tau_0}{\rho C\sigma_n} \tag{19}$$
$$\chi = \frac{\rho_s - \zeta\rho_f}{\rho_f\beta^\star}\frac{R^2}{\Lambda c_{th}}A_0$$
$$\psi = \frac{\rho_s\Delta H}{\rho C M_{CaCO_3}}\frac{R^2}{c_{th}}\frac{\Lambda}{\sigma_n}A_0,$$

and

$$\frac{\partial \gamma^p}{\partial t} = \frac{1}{H^\star}\left[\frac{\partial \sigma_{12}}{\partial t} + \frac{\sigma_{21}}{\partial t} + \mu\left(\frac{\sigma'_{11}}{\partial t}\right) + \frac{\sigma'_{22}}{\partial t}\right], \qquad (20)$$
$$H^\star = \frac{H}{\sigma_n} = h\frac{\sigma'}{\sigma_n}.$$

The corresponding dimensionless form of the linear and angular momentum with inertia and micro-inertia terms is as follows:

$$\begin{aligned} \frac{\partial \sigma_{12}}{\partial z} - I\frac{\partial^2 u_1}{\partial t^2} &= 0, \qquad (21)\\ \frac{\partial \sigma'_{22}}{\partial z} - \frac{\partial p}{\partial z} - I\frac{\partial^2 u_2}{\partial t^2} &= 0,\\ \frac{\partial m}{\partial z} + \sigma_{21} - \sigma_{12} - \frac{I}{2}\frac{\partial^2 \omega_c}{\partial t^2} &= 0, \end{aligned}$$

where $I = \frac{c_{th}^2 \rho_s}{R^2 \sigma_n}$ and the expressions of the stresses and couple stresses are derived from the elastoplastic model presented in Section 2.1 (Sulem et al. (2011)).

Following Vardoulakis and Sulem (1995) and Sulem et al. (2011), we introduce the perturbed fields (16) for a given initial configuration, and the spatial dependency of the perturbations is decomposed into Fourier modes with wavelength λ. Hence we introduce perturbations of the form

$$\begin{aligned} \tilde{u}_1(x_2,t) &= U_1 e^{st}\sin\left(\frac{z}{\lambda}\right), \qquad (22)\\ \tilde{u}_2(x_2,t) &= U_2 e^{st}\sin\left(\frac{z}{\lambda}\right),\\ \tilde{\omega}_c(x_2,t) &= \Omega e^{st}\cos\left(\frac{z}{\lambda}\right),\\ \tilde{p}(x_2,t) &= \Pi e^{st}\cos\left(\frac{z}{\lambda}\right),\\ \tilde{T}(x_2,t) &= \Theta e^{st}\cos\left(\frac{z}{\lambda}\right), \end{aligned}$$

with $\lambda = D/(\pi NR)$ and N equal to an integer satisfying the zero heat and fluid flux boundary conditions at $z = \frac{x_2}{R} = 0$. By substituting the perturbation fields (22) into the linearized governing equations (18, 21), we obtain a homogeneous algebraic system for the coefficients U_1,U_2,Ω,Π,Θ. A nonzero solution is possible only when the determinant of the linear system vanishes. This request results in a characteristic polynomial equation of degree 8 for the growth coefficient s. If a root has a positive real part, then the corresponding perturbation grows exponentially in time.

4.2. Numerical example

We consider the case of a 7-km deep fault, of a calcite-made gouge material having the parameters depicted in Table 4.2. With these values, and by performing the method presented in the Appendix A, we obtain a critical value for the hardening modulus $h_{cr} \approx 6$, such that for $h \geq h_{cr}$ all the roots of the polynomial equation have negative real part, and thus the system is stable. For $h < h_{cr}$ roots with positive real parts exist, bringing the system to instability.

We observe that the destabilizing effect of the chemical reaction by the fact that instability can occur in the hardening regime, for values of the hardening modulus significantly larger than in the case of thermal pressurization, $h'_{cr} = 0.014$ (Sulem et al. (2011)). Hence, as temperature increases reaching the activation temperature of the reaction, the material becomes unstable even at regimes mechanically considered as stable in the absence of chemical reaction.

In order to assess the localizing effect of the chemical reaction, we plot in the Appendix A the greatest root (i.e. the one corresponding to the insta-

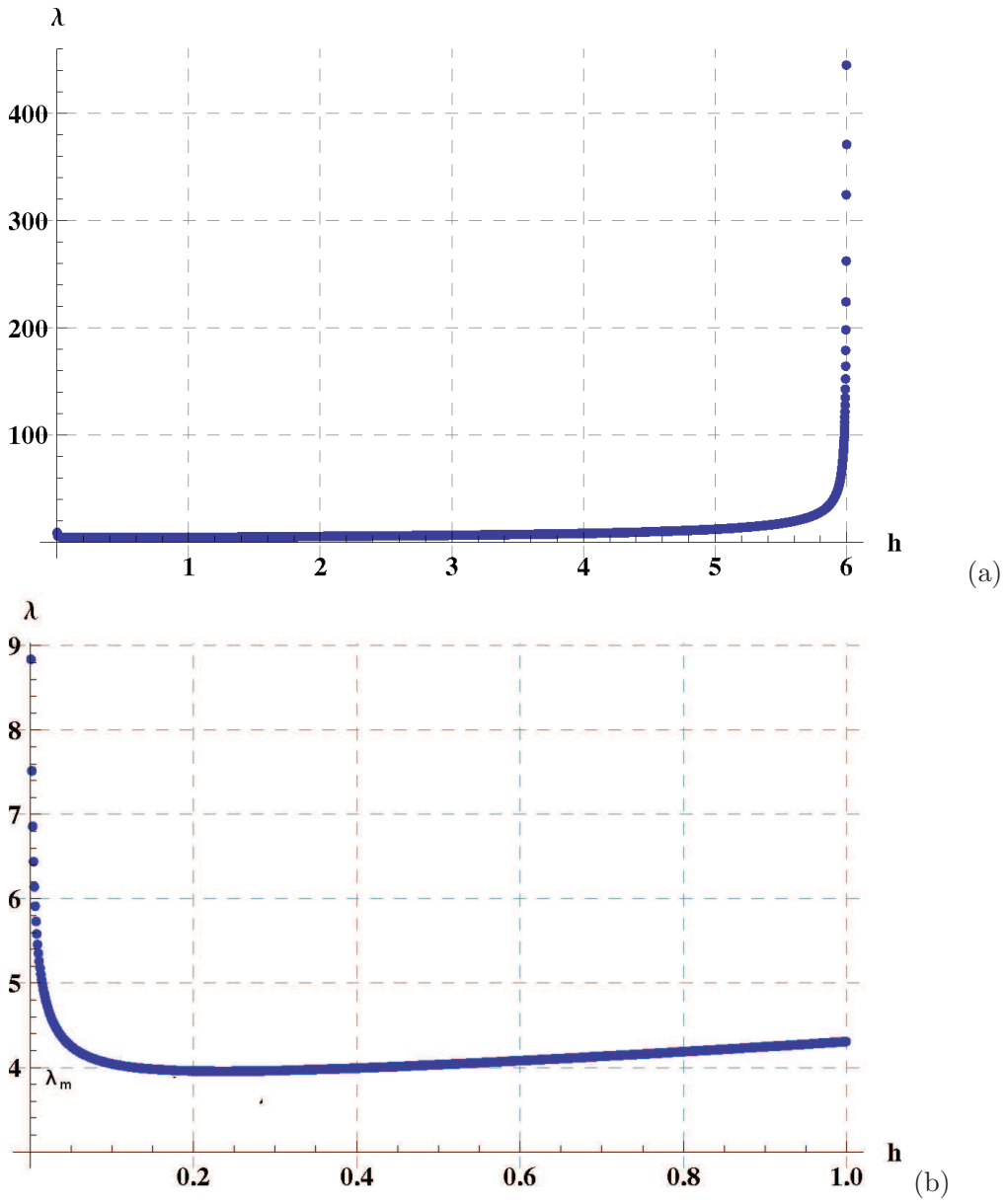

Figure 3: (a) Wave length λ corresponding to the fastest growth coefficient of the instability versus the hardening modulus h. (b) The same as in (a), focused in the area $0 < h < 1$, where the selected (minimum) wavelength, λ_m, is located. The results are calculated for $A_0 = 10^6$.

Parameter	Value	Units	Parameter	Value	Units
ϕ_0	0.03	–	c_{hy}	10^{-5}	m^2/s
σ'_n	200	MPa	c_{th}	10^{-6}	m^2/s
M_{CaCO_3}	0.1	kg/mol	R	0.1	mm
M_{CaO}	0.056	kg/mol	G	10^4	MPa
M_{CO_2}	0.044	kg/mol	K	$2 \cdot 10^4$	MPa
ρ_s	$2.5 \cdot 10^3$	kg/m^3	μ	0.5	–
ρ_f	10^3	kg/m^3	β	0	–
ρC	2.8	$MPa/°\mathrm{C}$	A_0	10^6	$1/s$
Λ	0.5	$MPa/°\mathrm{C}$	$\lvert\Delta H\rvert$	200	kJ/mol

Table 1: Indicative material parameters for a fault at 7 km depth, where the initial temperature is about 200°C. For these values of the parameters and for $T_c = 800°\mathrm{C}$ the corresponding dimensionles groups are $\zeta = 1.24$, $\alpha = 0.06$, $\delta = 0$, $\eta = 10$, $I = 1.25 \cdot 10^{-9}$, $\bar{\alpha}_s = 10^{-2}$, $\chi \approx 2A_0 = 2 \cdot 10^6$, $\psi \approx 0.01A_0 = 10^4$

bility mode with the fastest growth in time) as a function of the wavelength λ (Figure 6b) and select the wavelength number $\lambda = \lambda_m$ corresponding to the maximum value of the growth coeffcient s, so that a wavelength with the fastest growth in time appears. In Figure 3 this selected wavelength is plotted against the hardening modulus. As in Sulem et al. (2011) the selected wavelength tends to infinity for $h \to h_{cr}^-$ denoting that at initial instability no localization takes place. As the hardening modulus decreases the wavelength decreases as well, reaching a minimum at $h \approx 0.16$, where

$\lambda_m \approx 3.95$. Muhlhaus and Vardoulakis (1987) similarly obtained that at the bifurcation state the shear-band thickness for dry granular materials is infinite and decreases beyond the bifurcation state as the strain localization process evolves.

We notice that the selected wavelength ($\lambda_m \approx 3.95$) in this case is significantly smaller than in the absence of the chemical reaction ($\lambda'_m \approx 187$), revealing the crucial, localizing role of the chemical reaction. Since for this example we have used indicative values for the reaction parameters, like the pre-exponential factor and the activation temperature, we proceed with an analysis of these parameters in order to reveal their influence on the width of the PSZ and the type of instability.

5. Parametric Analysis. Impact of the chemical reaction and the pressurization mechanism

From the parameters appearing in 4.2, those being less constrained in values are the parameters of the reaction A_0 and T_c. Since they always appear in the parameter groups as a ratio A_0/T_c, we emphasize on the influence of this ratio on the stability of the system by treating it as a parameter.

5.1. Effect of the chemical reaction

To assess the influence of the chemical reaction, we plot in Figure 4 the values of h_{cr} with the ratio of the reaction parameters $\frac{A_0}{T_c}$ varying from 10^{-4} to 10^{12}. We observe that as $\frac{A_0}{T_c} \to 0$, then $h_{cr} \to h'_{cr} = 0.014$, thus it tends to the case of pressurization alone as weakening mechanism (Sulem et al. (2011)). As $\frac{A_0}{T_c}$ increases, h_{cr} increases as well, reaching an upper threshold at $h^m_{cr} \approx 6$.

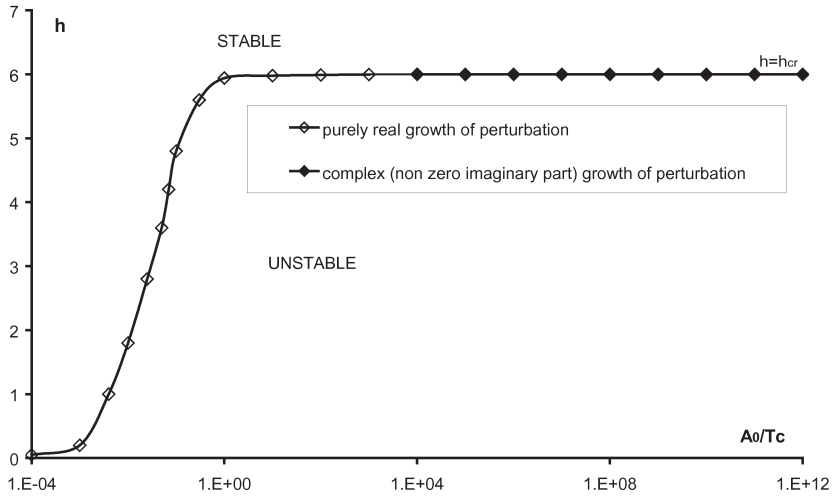

Figure 4: The critical hardening modulus h_{cr} as a function of A_0/T_c (logarithmic scale for A_0/T_c).

It is to be noted that as soon as h_{cr} reaches h_{cr}^{m}, then the maximum positive root changes from purely real to complex (Figure 4). This effect takes place at a critical $\frac{A_0}{T_c}$ (in this case $A_0^{cr} = 10^7\ s^{-1}$ for $T_c = 800°\text{C}$) and signifies the onset of oscillatory instabilities due to the chemical reaction. The existence of oscillatory instabilities is questionable because when the temperature decreases below the given threshold the reaction stops. In other words, the linear stability analysis is not valid for non monotonous processes in case of non-linear behaviour. For this reason the exact type of these oscillatory instabilities, as well as their time evolution cannot be determined by the present linear stability analysis. To this end nonlinear analyses and time integration of the full system of equations is required, to determine whether imaginary eigenvalues may correspond to stick-slip type of instability (appearing as limit cycles on a phase diagram, as for example in Alevizos and Veveakis (2011))

5.2. Effect of thermal pressurization mechanism

As already mentioned and anticipated, when $\frac{A_0}{T_c} \to 0$, then $h_{cr} \to h'_{cr} = 0.014$, thus the system is influenced by pressurization alone as weakening mechanism (Sulem et al. (2011)). However, when the reaction becomes strong and $\frac{A_0}{T_c}$ increases so that $h_{cr} \to h_{cr}^{m}$, the effect of thermal pressurization, compared to the chemical effect (i.e. the production of excess pore fluid due to $CaCO_3$ lattice breakdown and CO_2 production), is negligible. This fact becomes apparent in the Appendix A, where we compare the $s - \lambda$ curves of Figures 7b and 6b with the corresponding ones in the absence of thermal pressurization, appearing in Figure 8.

We notice that the same response is obtained, both for the magnitudes of

h, s and λ and for the type of instability (nodal instability for $A_0 = 10^6\ s^{-1}$ and oscillatory for $A_0 = 10^7\ s^{-1}$, $T_c = 800°\text{C}$). The pre-exponential factor for the considered depths cannot be realistically estimated, since it is pressure dependent (Lvov et al. (2002)) and there is a lack of experimental data at high pressures, however usually it is accepted to be more than $10^{10}\ s^{-1}$ (for example Dollimore et al. (1996) suggest a value of the order of $10^{15}\ s^{-1}$, used also by Sulem and Famin (2009)). Thus, we may conclude that at high temperatures where reaction is triggered (around T_c), and for the decomposition reaction considered, the main weakening mechanism of the two is the reaction, verifying the recent experimental findings of Han et al. (2007) and Ferri et al. (2010). However, as also discussed by Han et al. (2010) and De Paola et al. (2011) important weakening mechanisms like powder lubrication and flash heating (see also Rice (2006)) should not be excluded if one would like to model all the mechano-physical processes taking place in a fault, since they could have equal or even more dramatic role than chemical pressurization. In addition secondary chemo-mechanical effects like the breakdown of calcite grains expressed through the production of holes in the Calcite grains due to decarbonation reduce also the compressive strength, forcing the microstructure to collapse. In this study we have excluded these mechanisms to emphasize on the two pressurization mechanisms, i.e. thermal and chemical pressurization.

However, we notice that the initial temperature for a 7-km fault is around 200°C, far below the activation temperature $T_c \approx 800°\text{C}$ of calcite decomposition. Up to the temperature regime around T_c the reaction term is negligible and localization is driven by thermal pressurization, a fact that could not

be analyzed in this study due to the choice of the reference temperature T_c, around which we linearized in Section 4.1, in order to emphasize on the reaction itself. As temperature increases the process is progressively localizing towards an ultimate shear-zone whose thickness is determined by the reaction itself. To address this claim, we proceed with a shear band thickness analysis.

5.3. Shear band thickness, Wavelength selection

Indeed, it is expected that at temperatures near T_c the width D of the PSZ of Fig.1 is influenced by the chemical reaction. To verify this claim we may plot the minimum selected wavelength against the ratio A_0/T_c (Figure 5) to conclude that with increasing A_0/T_c, λ_m and thus D decrease. In the absence of chemical reaction, λ_m was calculated to be equal to about 187. The ultimate value for λ_m in the presence of a chemical reaction is around 3, denoting that the PSZ may be an extremely localized structure, obtaining $\lambda_m = 300\,\mu m$ when $d_{50} = 0.1\,mm$ as is the case for fine sands, or even less if we consider possible average grain sizes from principal slipping zones, up to $10\,\mu m$, in the lines of the field evidence provided by Smith et al (2011) and thoroughly discussed in the introduction.

Thus, indeed the onset of the reaction is taking place in an ultra localized zone, that could be significantly thinner than the initial one defined by thermal pressurization alone ($\lambda_m \sim 187$). This means that in a "non-reactive" fault thermal pressurization of pore fluids would result in a slipping zone of $18.7\,mm$ thick (for a fault material with $d_{50} = 0.1\,mm$), while under the same ambient conditions and slip rate, in a "reactive" gouge (e.g., calcite) chemical reaction would result in a slipping zone of $0.3\,mm$.

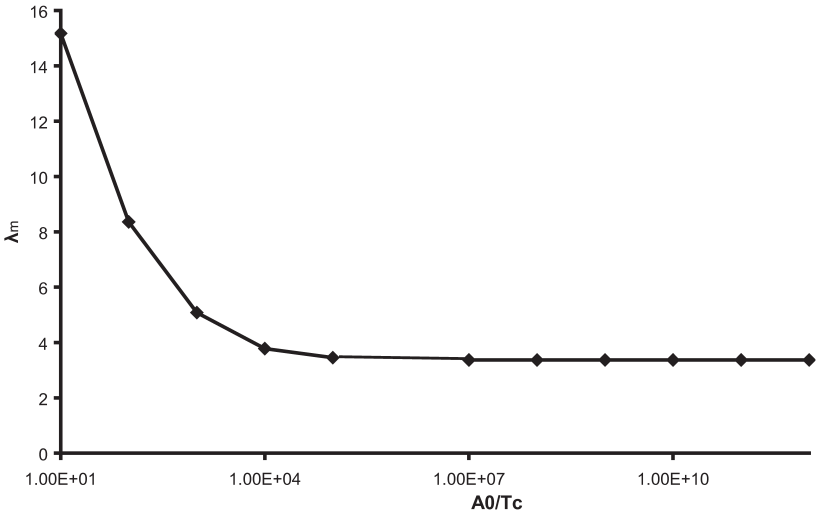

Figure 5: The selected wavelength λ_m as a function of A_0/T_c

What have to be noted at this point, is that localizing mechanisms like flash heating and breakage have been neglected in this study, as discussed thoroughly in Sections 2 and 5.2. Including these mechanisms would provide a more realistic behaviour of the fault even at low temperatures where pressurization or the chemical reaction are absent. In addition, the thickness of this ultimate structure (the PSZ) seems to push continuum theories to its limits, since the width of the structure is comparable to the size of the average grain. However, we emphasize that in this study the average grain size used (d_{50}) is the one of the initial grain size distribution and that during the evolution of a chemical reaction, grains undergo chemical degradation and phase transitions that could significantly alter the average grain size, or even make the determination of grain size ambiguous if amorphization (Yund et al (1990); Brantut et al. (2008)) is the chemical reaction. As shown by Veveakis et al. (2010); Alevizos and Veveakis (2011) during shearing of faults we may identify a regime of lower temperatures, where mechanical effects determine the evolution of the system and a high temperature regime, where the reaction is triggered and dominates the response of the fault, irrespective of the mechanical behavior. Thus, the present Cosserat approach is valid up to the point that chemical reaction is fully set and determines all the mechanical effects of the fault, like grain size evolutions and rheological response. It is used in order to obtain an estimate of the thickness of the layer at which chemical reaction will be triggered. Pass this point, either discrete analyses or even higher order continuum theories (Stefanou et al. (2010)) must be applied to account for the chemical reaction effects (for example by introducing varying d_{50}).

6. Discussion

Thermal instabilities were shown to be important at elevated temperatures, and to determine the stability of a fault even at regimes that are considered to be stable under purely mechanical conditions. The formalism presented here however revealed the importance of parameters that are not well-constrained. In particular, the hardening modulus h of rock materials is in principle varying with shear strain, while the parameters of the reaction A_0 and T_c strongly depend on the applied pressures at which the reaction takes place (Lvov (2007), pp. 79) and several values can be found in the literature (For example A_0 may vary from $10^2\, s^{-1}$ to $10^{20}\, s^{-1}$ for calcite decomposition, as discused by Lvov et al. (2002)).

Therefore, in order to apply the presented theory in real faults, there is a need of extensive laboratory testing of the strain-stress response of the fault gouge materials and on the effect of pressure and temperature on this response.

The results presented in this work could provide insight for the thermo-mechano-chemical coupling occurring in soil materials. Given the stress-strain response of the material, the ambient thermal conditions of the fault determine whether the fault may weaken thermally or not. At lower temperatures thermal pressurization may be triggered and cause softening at positive, but near zero, hardening modulus. At higher temperatures, near the activation of chemical reactions thermal softening induces a strong weakening effect since it may take place at extremely high (positive) values of the hardening modulus. Therefore at high temperatures even if the material is mechanically stable (steep hardening regime) the triggering of a chemical

reaction would lead the system to instability and softening.

The model presented here contains parameters that need to be evaluated from interdisciplinary experiments at conditions that match the ones met in real faults at seismic depths. Parameters like those appearing in the reaction rate of the chemical reaction (A_0, T_c) or in friction laws of geomaterials that would provide parameters like G_c should be evaluated before applying such models in real cases.

7. Conclusions

In this work, we have used higher order continua considerations and allowed to the fault material additional, rotational degree of freedoms, along with the presence of a decomposition reaction. We have shown that the ill-posed problem of simple shear of a saturated fault can be remedied when accounting for the micro-inertia of the rotations and that, at temperatures near its activation energy, the impact of the reaction is significant to the stability of the mechanical problem and the localization of deformation.

We have shown that the width of the localizing shear zone at which dynamic weakening of faults take place depends strongly on the parameters of the reaction, i.e. the pre-exponential factor A_0 and the activation temperature T_c. Small values of the ratio $\frac{A_0}{T_c}$ correspond to broader zones, of the order of few centimeters.

A. Linear Stability Analysis

By substituting the perturbation fields (22) into the linearized governing equations (18, 21), we obtain a homogeneous algebraic system for the

coefficients U_1,U_2,Ω,Π,Θ:

$$\begin{bmatrix} \frac{s\delta\sigma(d+\epsilon+2c\mu)}{2h\lambda\sigma'} & \frac{s\delta\sigma(2f+(a+b)\mu)}{2h\lambda\sigma'} & 0 & -\frac{a\alpha_s sT_c\delta\mu\sigma+\alpha_s bsT_c\delta\mu\sigma+2h\sigma'(sT_c+\chi)}{2hT_c\sigma'} & s+\frac{\eta}{\lambda^2} \\ -\frac{s\alpha\sigma(d+\epsilon+2c\mu)}{2h\lambda\sigma'} & \frac{s\alpha\sigma(2f+(a+b)\mu)}{2h\lambda\sigma'} & 0 & \frac{1}{\lambda^2}+\frac{s(a\alpha_s\alpha\mu]\sigma+\alpha_s b\alpha\mu]\sigma+2h\sigma')}{2h\sigma'}+\frac{\psi}{T_c} & 0 \\ -s^2I-\frac{d}{\lambda^2} & -\frac{f}{\lambda^2} & \frac{-d+\epsilon}{\lambda} & 0 & 0 \\ -\frac{c}{\lambda^2} & -s^2I-\frac{a}{\lambda^2} & 0 & \frac{\alpha_s(a+b)}{2\lambda} & \frac{1}{\lambda} \\ \frac{-d+\epsilon}{\lambda} & 0 & -2d+2\epsilon-\frac{s^2I}{2}-\frac{g}{\lambda^2} & 0 & 0 \end{bmatrix} \begin{bmatrix} U_1 \\ U_2 \\ \Omega \\ \Pi \\ \Theta \end{bmatrix} = 0, \tag{23}$$

where

$$\begin{aligned} a &= \frac{G+K-(\mu\beta K^2)/(G+H+K\beta\mu)}{\sigma}, \\ b &= \frac{K-G-(\mu\beta K^2)/(G+H+K\beta\mu)}{\sigma}, \\ c &= \frac{-(G\beta K)/(G+H+K\beta\mu)}{\sigma}, \\ d &= \frac{G+G_c-(G^2)/(G+H+K\beta\mu)}{\sigma}, \\ \epsilon &= \frac{G-G_c-(G^2)/(G+H+K\beta\mu)}{\sigma}, \\ f &= \frac{-(\mu GK)/(G+H+K\beta\mu)}{\sigma}, \\ g &= \frac{G}{\sigma}\ ,\ K = \frac{G}{1-2\nu}. \end{aligned} \tag{24}$$

A nonzero solution is possible only when the determinant of the linear system vanishes. This request results in a characteristic polynomial equation of degree 8 for the growth coefficient s. If a root has a positive real part, then the corresponding perturbation grows exponentially in time. Since a polynomial of degree 8 cannot admit an analytic solution, indicative values of the parameters have to be used in order to obtain numerical solutions

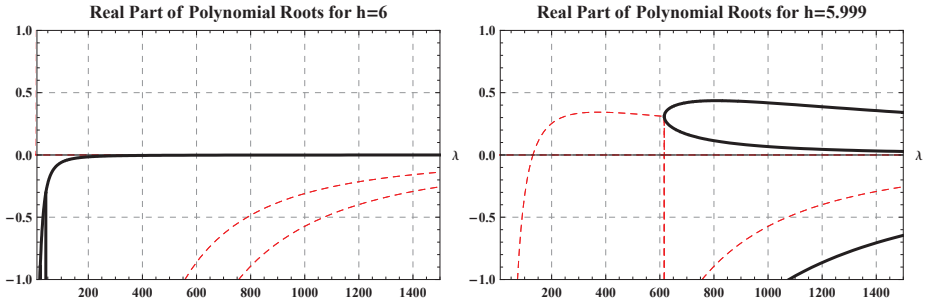

Figure 6: Real parts of the roots of the characteristic equation (growth coefficient s) as a function of the wavelength number λ, for $A_0 = 10^6$ and $T_c = 800$ (a) for $h \geq h_{cr} = 6$ where only negative roots appear, rendering the system stable, (b) for $h < h_{cr}$. The dashed curves represent the real part of complex roots whereas the solid curves depict the purely real roots (zero imaginary part). The wavelength at which the growth coefficient s obtains its maximum value is the one corresponding to the selected wavelength λ_m.

of the characteristic polynomial. To this end we consider the case of a 7-km deep fault, of a gouge material having the parameters depicted in Table 4.2. With these values we obtain a critical value for the hardening modulus $h_{cr} \approx 6$, such that for $h \geq h_{cr}$ all the roots of the polynomial equation have negative real part, and thus the system is stable (Figure 6a). For $h < h_{cr}$ roots with positive real parts exist, bringing the system to instability (Figure 6b).

In order to asses the localizing effect of the chemical reaction, we may plot the greatest root (i.e. the one corresponding to the instability mode with the fastest growth in time) as a function of the wavelength λ. This curve exhibits a maximum at $\lambda = \lambda_m$ so that a wavelength with the fastest growth in time appears (Figure 6b)

In the absence of thermal pressurization (i.e. when $\Lambda = 0$ in the original

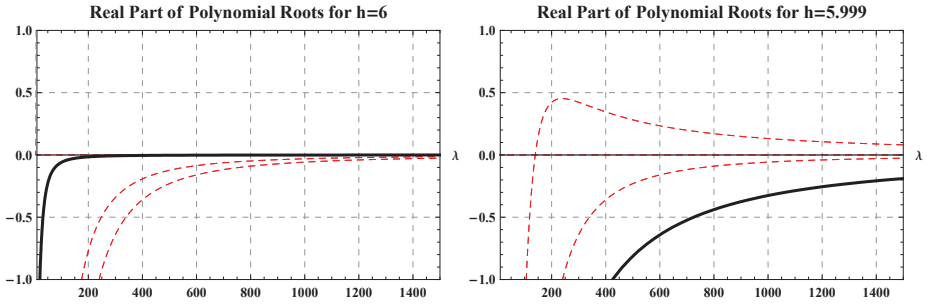

Figure 7: Real parts of the roots of the characteristic equation (growth coefficient s) as a function of the wavelength number λ, for $A_0 = 10^7$ and $T_c = 800$ (a) for $h \geq h_{cr} = 6$ where only negative roots appear, (b) for $h < h_{cr}$. The dashed curves represent the real part of complex roots, whereas the solid curves depict the purely real roots (zero imaginary part). The maximum root is complex in this case, denoting the onset of oscillatory instability.

set of equations), we rescale temperature with T_c, recalculate the roots of the characteristic polynomial and plot s against λ. By comparing the $s - \lambda$ curves of Figures 7b and 6b with the corresponding ones in the absence of thermal pressurization, appearing in Figure 8, we may conclude that thermal pressurization is a secondary effect at elevated temperatures where the reaction sets in.

Acknowledgments

The authors would like to thank G. Di Toro, N. Brantut and an anonymous reviewer for their comprehensive reviews and fruitfull comments, from which this paper has greatly benefited.

The research leading to these results has received funding from the European Research Council under the European Community's Seventh Framework Programme (FP7/2007-2013) / ERC grant agreement n 228051.

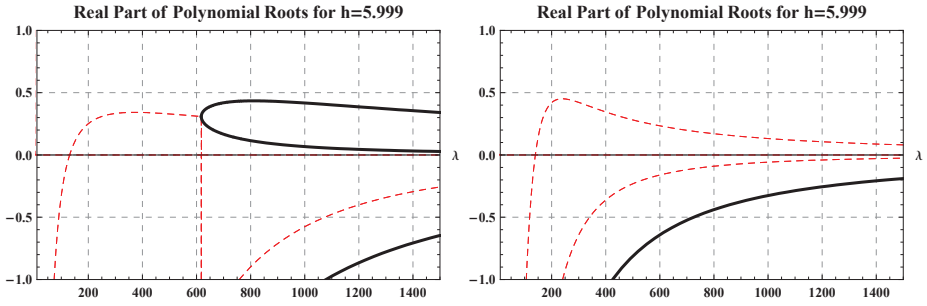

Figure 8: Real parts of the roots of the characteristic equation (growth coefficient s) as a function of the wavelength number λ, in the absence of thermal pressurization for $T_c = 800°\text{C}$ and (a) $A_0 = 10^6\ s^{-1}$, (b) $A_0 = 10^7\ s^{-1}$.

References

Alevizos, S., Veveakis, E., 2011. Thermal and chemical mechanisms of frictional faults: Static and dynamic instabilities. J. Mech. Phys. Solids in print.

Brantut, N., A. Schubnel, J.-N. Rouzaud, F. Brunet, and T. Shimamoto, 2008. High velocity frictional properties of a clay-bearing fault gouge and im- plications for earthquake mechanics, J. Geophys. Res., 113, B10401, doi: 10.1029/2007JB005551.

Brantut, N., Schubnel, A., Corvisier, J., Sarout, J., 2010. Thermochemical pressurization of faults during coseismic slip. J. Geophys Res. 115, B05314.

Brantut, N., Sulem, J., Schubnel, A., 2011. Effect of dehydration reactions on earthquake nucleation: Stable sliding, slow transients and unstable slip. J. Geoph. Res. 116, B05304, doi:10.1029/2010JB007876.

Brantut, N., R. Han, T. Shimamoto, N. Findling, and A. Schubnel, Fast

slip with inhibited temperature rise due to mineral dehydration: Evidence from experiments on gypsum, Geology, 39 (1), 5962, 2011.

Chester, F., 1995. A geologic model for wet crust applied to strike-slip faults. J. Geophys. Res. - Solid Earth 100, 13033–13044.

Chester, F., Chester, J., 1998. Ultracataclasite structure and friction processes of the punchbowl fault, san andreas system, california. Tectonophysics, 199–221.

Chester, F. M., Evans, J. P., Biegel, R. L., 1993. Internal structure and weakening mechanisms of the san andreas fault. J. Geophys. Res. 98, 771–786.

Chester, J. S., Goldsby, D. L., 2003. Microscale characterization of natural and experimental slip surfaces relevant to earthquake mechanics, SCEC Annu. Prog. Rep. 2003, South. Calif. Earthquake Cent., Los Angeles.

Chester, J.S., Chester, F.M., Kronenberg, A.K., 2005. Fracture surface energy of the Punchbowl Fault, San Andreas System. Nature 437, 133-136.

Cornet, F., Doan, M., Moretti, I., Borm, G., 2004. Drilling through the active Aigion fault: the aig10 well observatory. Comptes Rendus Geosciences 336 (4-5), 395–406.

Di Toro, G., Han R., Hirose, T., De Paola, N., Nielsen, S., Mizoguchi, K., Ferri, F., Cocco, M., Shimamoto, T., 2011. Fault lubrication during earthquakes. Nature, vol. 471, 494-498.

608 De Paola, N., Hirose, T., Mitchell, T., Di Toro, G., Togo, T., Shimamoto, T.
609 2011. Fault lubrication and earthquake propagation in thermally unstable
610 rocks. Geology, vol. 39, pp. 35-38.

611 Dollimore, D., P. Tong, and K. S. Alexander (1996), The kinetic interpreta-
612 tion of the decomposition of calcium carbonate by use of relationships
613 other than the Arrhenius equation, Thermochim. Acta, 282/283, 13 27.

614 Famin et al., 2008, Earthquakes produce carbon dioxide in crustal faults,
615 Earth and Planetary Science Letters, 265, 487-497.

616 Ferri, F., Di Toro, G., Hirose, T., Shimamoto, T., 2010. Evidence of ther-
617 mal pressurization in high-velocity friction experiments on smectite-rich
618 gouges. Terra Nova, 22: 347353, doi:10.1111/j.1365–3121.2010.00955.x.

619 Fisher, T.E. Tribochemistry. Ann. Rev. Mater. Sci. 18 303-323 (1988).

620 Garagash, D. I., Rudnicki., J. W., 2003a. Shear heating of a fluid-saturated
621 slip-weakening dilatant fault zone, 1, limiting regimes. J. Geophys. Res.
622 108.

623 Garagash, D. I., Rudnicki., J. W., 2003b. Shear heating of a fluid-saturated
624 slip-weakening dilatant fault zone, 2, quasi-drained regime. J. Geophys.
625 Res. 108.

626 Goren, L., Aharonov, E., 2007. Long runout landslides: The role of frictional
627 heating and hydraulic diffusivity. Geophys. Res. Lett. 34, L07301.

628 Goren, L., Aharonov, E., Anders, M. H., 2010. The long runout of the Heart

629 Mountain landslide:heating, pressurization, and carbonate decomposition.
630 J. Geophys. Res. 115, B10210.

631 Han, R., Shimamoto, T., Hirose, T., Ree, J., Ando, J., 2007. Ultralow friction
632 of carbonate faults caused by thermal decomposition. Science 316, 878–881.

633 Han, R., Hirose, T., and Shimamoto, T., 2010, Strong velocity weakening and
634 powder lubrication of simulated carbonate faults at seismic slip rate: Jour-
635 nal of Geophysical Research, v. 115, B03412, doi:10.1029/2008JB006136

636 Han, R. Takehiro Hirose, Toshihiko Shimamoto, Youngmin Lee and Jun-ichi
637 Ando, 2011, Granular nanoparticles lubricate faults during seismic slip,
638 Geology 2011;39;599-602

639 Hill, R., 1962. Acceleration waves in solids. J. Mech. Phys. Solids 10, 1–16.

640 Hirono, T. et al., 2007. A chemical kinetic approach to estimate dynamic
641 shear stress during the 1999 Taiwan Chi-Chi earthquake. Geophys. Res.
642 Lett. 34, L19308, doi:10.1029/2007GL030743.

643 Holcomb, D.J., Rudnicki, J.W., 2001. Inelastic constitutive properties and
644 shear localization in Tennessee marble, Int. J. Num. Anal. Meth. Geomech.
645 25, 109–129

646 Lachenbruch, A. H., Frictional heating, uid pressure, and the resistance to
647 fault motion, J. Geophys. Res., 85, 60976122, 1980.

648 Law, C., 2006. Combustion Physics. Cambridge University Press.

649 L'vov, B., 2007. Thermal Decomposition of Solids and Melts: New Ther-
650 mochemical Approach to the Mechanism, Kinetics and Methodology.
651 Springer.

652 L'vov, B. V., Polzik, L. K., Ugolkov, V. L., 2002. Decomposition kinetics
653 of calcite:a new approach to the old problem. Thermochimica Acta 390,
654 5–19.

655 Mandel, J., 1966. Conditions de stabilite et postulate de drucker. Rheology
656 and Soil Mechanics, 58–67.

657 Morgenstern, N. R., Tschalenko, J. S., 1967. Microscopic structures in kaolin
658 subjected to direct shear. Geotechnique 17, 309–328.

659 Muhlhaus, H. B., Vardoulakis, I., 1987. Thickness of shear bands in granular
660 materials. Geotechnique 37 (3), 271–283.

661 Nguyen, G. D., Einav, I., 2010. Nonlocal regularisation of a model based on
662 breakage mechanics for granular materials. Int. J. Sol. Struct. 47, 1350–
663 1360.

664 Noda, H., Shimamoto, T., 2005. Thermal pressurization and slip-weakening
665 distance of a fault: An example of the Hanaore fault, Southwest Japan.
666 Bull. Seismol. Soc. Am. 95 (4).

667 Pinyol, N., Alonso, E., 2010. Criteria for rapid sliding II.thermo-hydro-
668 mechanical and scale effects in Vaiont case. Engineering Geology 114,
669 211227.

Pittarello, L., Di Toro, G., Bizzarri, A., Pennacchioni, G., Hadizadeh, J., Cocco, M., 2008. Energy partitioning during seismic slip in pseudotachylyte-bearing faults (Gole Larghe Fault, Adamello, Italy). Earth and Planetary Science Letters, vol. 269, pp. 131-139.

Rice, J. R., 1975. On the stability of dilatant hardening for saturated rock masses. J. Geophys. Res. 80 (11), 1531 – 1536.

Rice, J. R., 2006. Heating and weakening of faults during earthquake slip. J. Geophys. Res. 111, B05311.

Rudnicki, J., Rice, J., 1975. Conditions for the localization of deformation in pressure sensitive dilatant materials. J. Mech. Phys. Solids 23, 371–394.

Sibson, R. H., Interaction between temperature and pore-uid pressure during earthquake faulting a mechanism for partial or total stress relief, Nature, 243, 6668, 1973.

Sibson, R.H., Thickness of the Seismic Slip Zone, Bull. Seism. Soc. Am., 93, 1169-1178, 2003.

Smith, S. A. F., A. Billi, G. Di Toro, and R. Spiess, Principal slip zones in limestone: Microstructural characterization and implications for the seismic cycle (Tre Monti fault, Central Apennines, Italy), Pure Appl. Geophys., doi:10.1007/s00024-011-0267-5, 2011.

Sulem, J., 2007. Stress orientation evaluated from strain localisation analysis in Aigion fault. Tectonophysics 442, 3–13.

691 Sulem, J., Famin, V., 2009. Thermal decomposition of carbonates in fault
692 zones: slip-weakening and temperature-limiting effects. J. Geophys. Res.
693 114, B03309.

694 Sulem, J., Stefanou, I., Veveakis, E., 2011. Stability analysis of undrained
695 adiabatic shearing of a rock layer with Cosserat microstructure. Granular
696 Matter in press, doi:10.1007/s10035–010–0244–1.

697 Sulem, J., Vardoulakis, I., Ouffroukh, H., Perdikatsis, V., 2005. Thermo-
698 poro-mechanical properties of the aigion fault clayey gouge - application
699 to the analysis of shear heating and fluid pressurization. Soils and Foun-
700 dations 45, 97–108.

701 Stefanou I., Sulem J. and Vardoulakis I., 2010. Homogenization of inter-
702 locking masonry structures using a generalized differential expansion tech-
703 nique. International Journal of Solids and Structures 47, 1522–1536.

704 Tisato, N., Di Toro, G., De Rossi, N., Quaresimin, M., Candela T., 2011.
705 Experimental investigation of flash weakening in limestone. Submitted to
706 Journal of Structural Geology.

707 Yue, L., Shui, M. and Xu, Z. The decomposition kinetics of nanocrystalline
708 calcite. Thermochimica Acta 335 121-126 (1999).

709 Yund, R. A., M. L. Blanpied, T. E. Tullis, and J. D. Weeks, Amorphous ma-
710 terial in high strain experimental fault gouges, J. Geophys. Res., 95 (B10),
711 15,58915,602, 1990.

712 Vardoulakis, I., 1985. Stability and bifurcation of undrained, plane rectilin-
713 ear deformations on water-saturated granular soils. Int. J. Numer. Anal.
714 Methods Geomech. 9, 339–414.

715 Vardoulakis, I., 1986. Dynamic stability of undrained simple shear on water-
716 saturated granular soils. Int. J. Numer. Anal. Methods Geomech. 10, 177–
717 190.

718 Vardoulakis, I., 1996. Deformation of water-saturated sand: II. effect of pore
719 water flow and shear banding. Geotechnique 46 (3), 457–472.

720 Vardoulakis, I., 2002a. Dynamic thermo-poro-mechanical analysis of catas-
721 trophic landslides. Geotechnique 52, 157–171.

722 Vardoulakis, I., Sulem, J. (Eds.), 1995. Bifurcation Analysis in Geomechan-
723 ics. Blankie Acc. and Professional.

724 Veveakis, E., Alevizos, S., Vardoulakis., I., 2010. Chemical reaction capping
725 of thermal instabilities during shear of frictional faults. J. Mech. Phys.
726 Solids 58, 1175 – 1194.

727 Veveakis, E., Vardoulakis, I., Di Toro., G., 2007. Thermoporomechanics of
728 creeping landslides: The 1963 Vaiont slide, Northern Italy. J. Geophys.
729 Res. 112, F03026.

730 Wibberley, C., Shimamoto, T., 2005. Earthquake slip weakening and asperi-
731 ties explained by thermal pressurization. Nature 426 (4), 689–692.

732 Wibberley, C. A. J., Shimamoto, T., 2003. Internal structure and perme-

733 ability of major strike-slip fault zones: The median tectonic line in mid
734 prefecture, southwest japan. J. Struct. Geol. 25, 59–78.

735 Wibberley , C.A.J, Graham, Y., Di Toro, G., 2008. Recent advances in the
736 understanding of fault zone internal structure: a review. In "The Internal
737 Structure of Fault Zones - implications for mechanical and fluid flow prop-
738 erties", Eds. C.A.J. Wibberley, W. Kurz, J. Imber, R.E. Holdsworth and
739 C. Collettini, Special Volume of the Geological Society of London, Vol.
740 299, pp. 5-33.